Synthesis, characterization and corrosion inhibition potential of two novel Schiff bases on mild steel in acidic medium†

Archana Pandey,*[a] B. Singh,[a] Chandrabhan Verma[bc] and Eno E. Ebenso ⓘ *[bc]

The present study deals with the synthesis of two novel Schiff bases (SBs) namely; 5-((4-chloro-3-nitrophenylimino)methyl)-2-methoxyphenol (**SB-1**) and 2-(4-hydroxy-3-methoxybenzylidineamino)-4-nitrophenol (**SB-2**) using a solid–liquid phase equilibrium diagram and their characterization *via* ^{1}H and ^{13}C NMR, FT-IR and UV-vis spectral analyses. Differential scanning calorimetric (DSC) thermographs were also obtained to further support the synthesis and identify the melting temperatures of **SB-1** and **SB-2**. The XRD technique was employed to study the atomic packing, crystal structure and space group of the grown crystals of **SB-1**. Results showed that powder X-ray diffraction patterns of both SBs are entirely different than those of their corresponding starting compounds. The inhibition properties of the investigated SBs were evaluated for mild steel corrosion in 1 M HCl using electrochemical impedance spectroscopy (EIS), potentiodynamic polarization (PDP) and computational (DFT) methods. Electrochemical and DFT studies revealed that the tested SBs act as good inhibitors for acidic corrosion of mild steel and their efficiency increases ($\eta\%$) on increasing their concentrations. Electrochemical results revealed that **SB-1** and **SB-2** showed maximum inhibition efficiencies of 95.58% and 96.80%, respectively, at a concentration as low as 0.327 mM. Results from a polarization study suggest that the studied SBs act as mixed type corrosion inhibitors with some cathodic predominance. The DFT based parameters such as E_{HOMO}, E_{LUMO}, ΔE, electronegativity (χ), hardness (η), softness (σ) and the fraction of electron transfer (ΔN) were calculated to corroborate the experimentally obtained results. Both experimental and DFT results were in good agreement.

1. Introduction

Mild steel is a widely employed construction material owing to its high mechanical strength and exceptionally low cost.[1–3] However, it rapidly undergoes corrosion through chemical and electrochemical reactions with the components of surrounding environments. Corrosion is an extremely damaging phenomenon and adversely affects the global economy of the world. A study of the National Association of Corrosion Engineers (NACE; 2002) revealed that in 1998, the total direct cost of corrosion was US $276 billion, which constitutes about 3.4% of the world's GDP.[4] In the United States (U. S.), corrosion resulted in a loss of more than US $2.2 trillion in 2011. According to the 1$^{\text{st}}$ Global Corrosion Summit held in New Delhi, India in 2011, India losses around Rs. 2 lakh crores (US $45 billion) every year because of corrosion.[5] The most cited cost study data of NACE suggests that recent annual cost of corrosion (worldwide) is about US $2.5 trillion which results nearly 3.4% of the global GDP.[6,7] In India and South Africa the total annual cost of corrosion is around US $100-billion and US $ 9.6 billion, respectively.[6,7] However, several attempt such as coating, alloying, de-alloying and use of synthetic corrosion inhibitors *etc.* being made to reduce this cost of corrosion by implementing them the cost of corrosion can be reduced from 15 (US $ 375 billion) to 35% (US $ 875 billion).

Among the available methods of corrosion protection, use of synthetic inhibitors is one of the most popular and effective methods due to their cost effective nature and ease of application.[1–3,8–10] These inhibitors adsorb on the metallic surface through their non-bonding and pi-electrons and form protective film which isolates the metals from the corrosive environment and protects from corrosion.[8–10] The adsorption of these inhibitors depends upon numerous factors such as nature of metal and electrolyte, electronic structure of the inhibitor, temperature, exposure time *etc.*[11,12] Recently, widespread studies of organic compounds show that these compounds exhibit various attractive linear and non-linear optical properties.[13,14] Schiff bases are

[a]Department of Chemistry, Centre of Advance Study, Institute of Science, Banaras Hindu University, Varanasi-221005, India. E-mail: archana.pandey2504@gmail.com
[b]Department of Chemistry, School of Chemical and Physical Sciences, Faculty of Natural and Agricultural Sciences, North-West University, Private Bag X2046, Mmabatho 2735, South Africa. E-mail: Eno.Ebenso@nwu.ac.za
[c]Material Science Innovation & Modelling (MaSIM) Research Focus Area, Faculty of Natural and Agricultural Sciences, North-West University, Private Bag X2046, Mmabatho 2735, South Africa

† Electronic supplementary information (ESI) available. See DOI: 10.1039/c7ra08887f

generally synthesized by condensation reaction between aromatic aldehyde and primary amine (–HC=N–). They have been extensively used for variety of biological applications in the field of pharmaceuticals.[15–18] They have also been used as promising candidates for antimicrobial activity[19] such as antibacterial, antifungal, antitumor and anticancer agents.[20] They are also being utilized as common and effective intermediate candidates for the synthesis of several organic and coordination compounds.[21] Additionally, the Schiff bases are also being utilized as fluorescent probe,[13,22–24] non-linear optical (NLO) active,[25] catalyst, dyes and inhibitors for metallic corrosion[26] *etc.* Owing to their cost effective nature, high synthetic yield, low toxicity and high chemical purity, Schiff bases (SBs) are ideal candidates to be used for a variety of purposes like agents for antimicrobial and anticorrosive activities. The presence of –CH=N– group in their molecular structures makes them suitable candidates for several applications in medicinal, agricultural, pharmaceutical and material science. Previously, several Schiff bases have been prepared by condensation reactions of carbonyl and amine compounds. Literature survey reveals that several Schiff's bases have been employed as effective corrosion inhibitors for metals and alloys using experimental and computational methods in different aggressive media.[27–29] Their high effectiveness and adsorption tendency on the metallic surfaces mainly attributed to the presence of –CH=N– (imine) group through which they can adsorb effectively *i.e.* –CH=N– group acts as an adsorption canter during meta-inhibitor interactions.[27–29] A comparison of inhibitive strengths of 2-amino-6-(4-methoxybenzelideneamino)hexanoic acid (SB-2-M) and 2-amino-6-((4-dimethylamino)benzylideneamino)hexanoic acid (SB-4-D) having *p*-OCH$_3$ and *p*-N(CH$_3$)$_2$, respectively showed that SB-4-D is a better inhibitor than SB-2-M.[27] The higher inhibition efficiency of SB-4-D is attributed due to more electron releasing nature of –NMe$_2$ as compared to –OCH$_3$ group of SB-2-M. 4-Hydroxy-3-methoxybenzaldehyde (vanillin) is the major chemical ingredient of vanilla and is generally used as flavor in sweet, beverages, pharmaceuticals, food and perfumery industries because of its desirable flavor and fragrance properties.[30] Schiff's bases obtained from vanillin have been verified to take many functional groups that act as chelating legends[31] and potential as antibacterial agents against some bacterial strains.[32] 4-Chloro-3-nitroaniline is used as Schiff bases synthesis as well as conformers in co-crystals.[33] 2-Amino-4-nitrophenol derived Schiff base known for anion sensor,[34] fluorescent chemosensor[35] and related metal complexes for the cytotoxic agent.[36] 3-Hydroxy-4-methoxybenzaldehyde Schiff base metal complexes are reported for biological activity.[37]

Herein, considering the different applications and importance of Schiff bases, we report for the first time in literature synthesis and characterization of two novel Schiff bases based on 3-hydroxy-4-methoxybenzaldehyde, 4-chloro-3-nitroaniline, 4-hydroxy-3-methoxybenzaldehyde (vanillin) and 2-amino-4-nitroaniline namely, 5-((4-chloro-3-nitrophenylimino)methyl)-2-methoxyphenol (**SB-1**) and 2-(4-hydroxy-3-methoxybenzylidineamino)-4-nitrophenol (**SB-2**) *via* solid–liquid phase equilibrium diagram study. Literature survey reveals that previously some of the Schiff bases have been evaluated as corrosion inhibitors for metals and alloys in different electrolytic media which showed the inhibition

efficiency of 70–98% at as high as 350–2700 ppm concentrations.[38–40] In view of this observation, in the present study we tested the inhibition performance of investigated SBs and observed that both the SBs showed more than 95% efficiency at 0.327 mM concentration. The synthesized SBs were characterized by spectral techniques such as ^{1}H and ^{13}C NMR, and FT-IR analysis. Optical properties were investigated by UV-vis absorption and fluorescence in methanol. Thermal properties, melting temperature, stability and decomposition study of the **SB-1**, 3-hydroxy-4-methoxybenzaldehyde, 4-chloro-3-nitroaniline, **SB-2**, 4-hydroxy-3-methoxybenzaldehyde and 2-amino-4-nitrophenol compounds have been studied using DSC and TGA. The effect of the synthesized SBs concentration on mild steel corrosion in 1 M HCl has been investigated using experimental and DFT approaches.

2. Experimental section

2.1. Materials and methods

3-Hydroxy-4-methoxybenzaldhyde (HMB) (99%), 4-chloro-3-nitroaniline (CNA) (≥97%), 2-amino-4-nitrophenol (ANP) (≥98%) and 4-hydroxy-3-methoxybenzaldehyde (vanillin, V) (99%) were obtained from Sigma-Aldrich. All chemicals were used for the synthesis of Schiff bases, without further purification.

2.2. Phase diagram

Solid–liquid phase equilibrium diagram of 4-chloro-3-nitroaniline (1)–3-hydroxy-4-methoxybenzaldehyde (2) and 4-hydroxy-3-methoxybenzaldehyde (1)–2-amino-4-nitrophenol (2) systems have been studied by thaw–melt method as earlier reported.[41–43] Melting temperatures of synthesized materials were determined by using a melting point (Toshniwal melting point) apparatus.

For electrochemical measurements, mild steel specimens having chemical composition (wt%): C (0.076), Mn (0.192), P (0.012), Si (0.026), Cr (0.050), Al (0.023), and Fe (balance; 99.62) was used as test material. The 1 M HCl was used as electrolytic medium for electrochemical measurements of the investigated SBs. The metallic specimens were abraded with emery paper of different grades in order to clean their surface followed by their washing with double deionized water, ultrasonic cleaning in ethanol and finally degreasing with acetone. The cleaned metallic specimens were dried under hot air blower and stored in desiccators before use.

2.3. DSC and TGA analyses

Melting temperature and heat of fusion of both the SBs and eutectics as well as their starting components have been determined using differential scanning calorimetry (DSC) (Mettler DSC-4000 system). Before starting the experiment, DSC unit was calibrated using the indium metal as a standard. DSC and TGA experiments were performed under gaseous environment of nitrogen and the gas flow rate was maintained throughout the measurements. Test sample (4–6 mg) was carefully measured in aluminum pan and further sealed which was heated at rate of 10 °C min^{-1}. Enthalpy of fusion was obtained and reproducible within ±0.01 kJ mol^{-1}. Thermal

stability of both the SBs was demonstrated by thermo gravi-metric analysis. TGA was performed using a Perkin-Elmer STA 6000 thermal analyzer in the temperature range 303 to 800 K at heating rate 10 °C min⁻¹. The samples were purged with a stream of flowing nitrogen throughout the experiments.

2.4. Spectral studies

^{1}H and ^{13}C NMR spectra of both the Schiff's bases and starting materials were recorded in CDCl$_3$ using JOEL AL300 MHz spectrometer using tetra-methyl silane (TMS) as internal reference. FT-IR analysis of both the SBs was carried out using Perkin Elmer FT-IR Spectrum, 1000 Infrared spectrometer. During FT-IR experiment, samples were pelletized with KBr. FT-IR spectra of SBs and starting materials were recorded at 300 K in 4000–400 cm⁻¹ region.

2.5. Powder X-ray diffraction (PXRD)

Crystalline behaviour and diffraction patterns of the SBs were determined using the powder X-ray diffraction (PXRD). The X-ray diffraction (XRD) technique has been utilized for the identification of the nature of eutectics shown in the phase diagrams. The PXRD patterns of eutectics of the synthesized SBs and their starting chemicals were recorded using an 18 kW rotating (Cu) anode based Rigaku powder diffractometer fitted with a graphite mono-chromator in the diffracted beam. The very fine powdered samples were scanned from 10° to 70° with at the scan rate of 4° min⁻¹.

2.6. Single crystal XRD

Structural analysis of SBs undertaken in present study was also carried out using single crystal XRD by grown single crystals of **SB-1**. The saturated solution of **SB-1** was prepared in mixed (methanol and water) solvent at room temperature and slow evaporation method was used for single crystals growth. After few days fine needle shaped (yellowish) single crystals were harvested. We have made several attempts in order to find the single crystals for **SB-2** but unlike to **SB-1**, it gives very poor crystalline behaviour at room temperature. The single crystal X-ray diffraction pattern of **SB-1** was recorded using the X Caliber Oxford CCD diffractometer. The data detection was carried out using Chrysalis Pro software. The structure solution and refinement were studied utilizing SHELXS and SHLEXL-97.[44]

2.7. UV-vis absorption and emission studies

UV-vis absorption of **SB-1**, **SB-2** compounds and 3-hydroxy-4-methoxybenzaldehyde, 4-chloro-3-nitroaniline, 4-hydroxy-3-methoxybenzaldehyde and 2-amino-4-nitrophenol have been recorded in methanol at 1×10^{-5} M concentration using JASCO V-670 absorption spectrophotometer in 200–900 nm range. The fluorescence spectra of SBs have been measured in methanol at 1×10^{-5} M concentration using Varian Cary Eclipse fluorescence spectrophotometer.

2.8. Electrochemical measurements

The electrochemical behaviour of synthesized Schiff's bases was investigated using GamryPotentiostat/Galvanostat (Model G-300) instrument embedded with Analyst 5.0 software. A conventional three electrodes cell containing saturated calomel (reference electrode; RE), graphite rod (counter electrode; CE) and mild steel specimens (working electrode; WE) were used for all electrochemical measurements. Potentiodynamic polarization studies were done by changing the WE potential from −250 mV to +250 mV with respect to the potential of RE at a perpetual sweep rate of 1.0 mV s⁻¹. The current density (i_{corr}) was derived by extrapolation of Tafel curves through which inhibition efficiency was derived using following equation:[9,12]

$$\eta\% = \frac{i_{corr}^0 - i_{corr}^i}{i_{corr}^0} \times 100 \qquad (1)$$

where, i_{corr}^0 and i_{corr}^i are corrosion current densities in the absence and presence of inhibitors, respectively. EIS studies were performed at the open circuit potential (OCP) in frequency range of 100 kHz to 0.01 Hz through AC current input having amplitude 10 mV peak to peak. The inhibition efficiency was calculated from polarization resistance (R_p; obtained from Nyquist plots) using following relationship:[9,12,45]

$$\eta\% = \frac{R_p^i - R_p^0}{R_p^i} \times 100 \qquad (2)$$

where, R_p^0 and R_p^i are polarization resistances in the absence and presence of inhibitors, respectively. DFT studies were performed using Gaussian 09 software as described earlier.[12,43,44] Several outputs and descriptors such as energies of highest and lowest unoccupied molecular orbitals (E_{HOMO}, E_{LUMO}), energy band gap (ΔE), electronegativity (χ), global hardness (η), softness (σ), and fraction of electron transfer (ΔN) have been calculated using following relationships:[12,46–48]

$$\Delta E = E_{LUMO} - E_{HOMO} \qquad (3)$$

$$\eta = \frac{1}{2}(E_{LUMO} - E_{HOMO}) \qquad (4)$$

$$\chi = -\frac{1}{2}(E_{LUMO} + E_{HOMO}) \qquad (5)$$

$$\Delta N \frac{\chi_{Fe} - \chi_{inh}}{2(\eta_{Fe} + \eta_{inh})} = \frac{\phi - \chi_{inh}}{2(\eta_{Fe} - \eta_{inh})} \qquad (6)$$

where, χ_{Fe} and η_{inh} denote the electronegativity and hardness of iron and inhibitor, respectively. A value of 0.2572 hartree was used for the χ_{Fe}, while η_{Fe} was taken as 0 hartree for bulk Fe atom in accordance with the Pearson's electronegativity scale.[12,46–48] In the present study, value of χ_{Fe} is replaced by its work function (ϕ) as described earlier.[49–53] The values of ϕ derived from DFT calculations which are 0.1436, 0.1771 and 0.1425 hartree for the Fe (100), Fe (110) and Fe (111), respectively. In present study we chosen Fe (110) surface because of its high stabilization energy and highly packed structure.

3. Results and discussion

3.1. Phase diagram

Solid–liquid phase equilibrium diagram of 4-chloro-3-nitroaniline (1)–3-hydroxy-4-methoxybenzaldehyde (2) and 4-
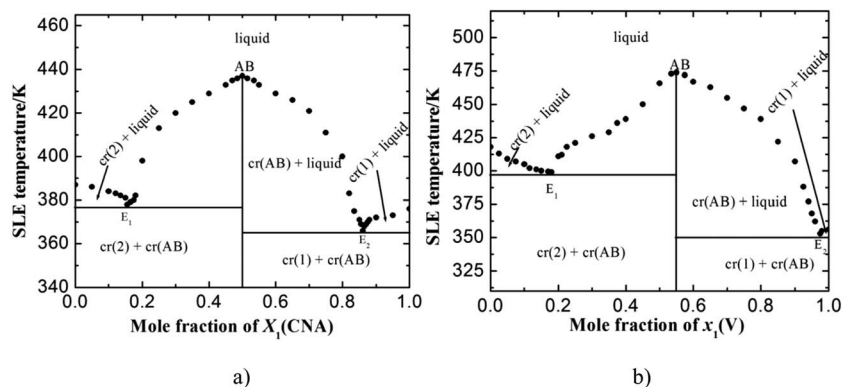
Fig. 1 Solid–liquid phase equilibrium diagram of (a) 4-chloro-3-nitroaniline (1)–3-hydroxy-4-methoxybenzaldehyde (2) and (b) 4-hydroxy-3-methoxybenzaldehyde (1)–2-amino-4-nitrophenol (2) systems.

hydroxy-3-methoxybenzaldehyde (1)–2-amino-4-nitrophenol (2) systems are reported in the term of melting temperature-composition curves (Fig. 1a and b). In each case, SBs formation occurs in 1 : 1 molar ratio of their starting chemicals with congruent melting temperature and two eutectics E_1 and E_2 as depicted in the phase diagram. In the case of 4-chloro-3-nitroaniline (1)–3-hydroxy-4-methoxybenzaldehyde (2) system, eutectic E_1 and E_2 were found at 0.155 and 0.860 mole fraction of component (1), respectively. The melting temperature of SB-1, E_1 and E_2 were obtained 439, 377 and 367 K, respectively (Fig. 1a). In the diagram, melting temperature of starting compound, 3-hydroxy-4-methoxybenzaldehyde decrease with addition of 4-chloro-3-nitroaniline and reaches to the minimum melting point which is the first eutectic point (E_1) and further addition of second mixture component CNA melting temperature increases and reaches up to maximum value of 439 K which is the congruent melting temperature of SB-1. Further increase in the amount of CNA decreases value of melting temperature and finally reaches minimum value of 367 K which is second eutectic point (E_2). Similarly, in case of 4-hydroxy-3-methoxybenzaldehyde (1)–2-amino-4-nitrophenol (2) system, E_1 and E_2 was obtained at 0.180, 0.975 mole fraction of vanillin,

respectively. Melting temperature for SB-2, E_1 and E_2 are 474, 399 and 353 K, respectively. Both the synthesized compounds are pure in nature and behave as one of the parent component for both eutectics (E_1 and E_2).

3.2. Differential scanning calorimetry (DSC)

Melting temperatures and heat of fusion for the SB-1 and SB-2 and eutectics were determined with the help of DSC. DSC curves of 4-chloro-3-nitroaniline (1)–3-hydroxy-4-methoxybenzaldehyde (2) and 4-hydroxy-3-methoxybenzaldehyde (1)–2-amino-4-nitrophenol (2) systems are shown in Fig. 2a and b. The endothermic peaks in DSC indicate that the melting temperature of the SB-1, SB-2 and eutectics. DSC studies provide the information about the phase transitions, in both the cases SB-1, SB-2 and relative eutectics not show additional phase transitions in DSC curves. DSC study provide precise and clear melting point of SB-1 and SB-2 compounds and eutectics, sharp endotherm indicates that the purity of compounds. Furthermore, the various thermal parameters have been computed using DSC data such as enthalpy of fusion, heat of mixing, entropy of fusion and roughness parameters using mixture law and are presented in Table 1. The enthalpy of mixing was found negative (Table 1) in each eutectic of 4-chloro-
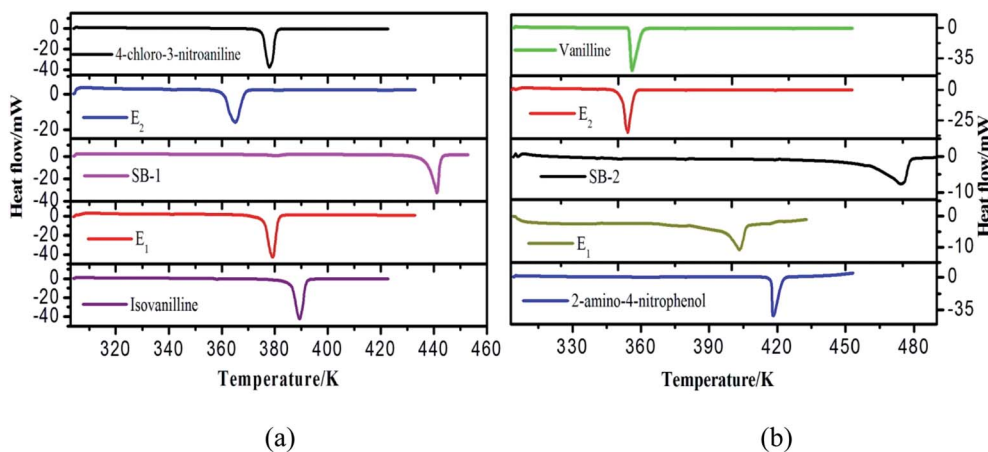

Fig. 2 DSC curves of (a) 4-chloro-3-nitroaniline (1)–3-hydroxy-4-methoxybenzaldehyde (2) and (b) 4-hydroxy-3-methoxybenzaldehyde (1)–2-amino-4-nitrophenol (2) systems.

3-nitroaniline (1)–3-hydroxy-4-methoxybenzaldehyde (2) and 4-hydroxy-3-methoxybenzaldehyde (1)–2-amino-4-nitrophenol (2) systems suggesting that clustering of appropriate molecules.[54] The excess thermodynamics function such as excess free energy (g^E), excess enthalpy (h^E) and excess entropy (s^E) for eutectic composition were computed by using eqn (7)–(9) as reported earlier,[50]

$$g^E = RT[x_1 \ln \gamma_1^1 + x_2 \ln \gamma_2^1] \quad (7)$$

$$h^E = -RT^2 \left[x_1 \frac{\partial \ln \gamma_1^1}{\partial T} + x_2 \frac{\partial \ln \gamma_2^1}{\partial T} \right] \quad (8)$$

$$s^E = -R \left[x_1 \ln \gamma_1^1 + x_2 \ln \gamma_2^1 + x_1 T \frac{\partial \ln \gamma_1^1}{\partial T} + x_2 T \frac{\partial \ln \gamma_2^1}{\partial T} \right] \quad (9)$$

where, $\ln \gamma_i^1$, x_i and $\frac{\ln \gamma_i^1}{\partial T}$ respectively represent the activity coefficients in the liquid state, the mole fraction and the variation of log of activity coefficient in liquid state as a function of temperature for the component i. Activity coefficient (γ_i^1) can be evaluated using the equation below,[50]

$$-\ln\left(x_i \gamma_i^1\right) = \frac{\Delta_{fus} H_i}{R} \left(\frac{1}{T_{fus}} - \frac{1}{T_i} \right) \quad (10)$$

where, x_i, $\Delta_{fus} H_i$, T_i and T_{fus} are mole fraction, enthalpy of fusion, melting temperature of component i and melting temperature of eutectics, respectively. The variation of activity coefficient with temperature can be computed using differentiating the eqn (11) given below:

$$\frac{\partial \ln \gamma_1^1}{\partial T} = \frac{\Delta_{fus} H_i}{RT^2} - \frac{\partial x_i}{x_i \partial T} \quad (11)$$

where, value of $\partial x_i / \partial T$ in the above equation can be evaluated by allowing for two nearest points of eutectic composition. In case of 4-hydroxy-3-methoxybenzaldehyde (1)–2-amino-4-nitroaniline (2) system, positive value of excess free energy was found at both the eutectics indicating that an association

Table 1 Heat of fusion, entropy of fusion and roughness parameter of starting components, complexes (SB-1 and SB-2) and their eutectics

Materials		Enthalpy of fusion (kJ mol^{-1})	Heat of mixing (kJ mol^{-1})	Entropy of fusion (kJ mol^{-1} K^{-1})	Roughness parameter
HMB		26.70		0.069	8.299
CNA		34.03		0.090	10.825
E$_1$	(Exp.)	27.98	−2.29	0.074	8.900
	(Cal.)	30.27			
E$_2$	(Exp.)	23.47	−11.73	0.064	7.697
	(Cal.)	35.20			
SB-1	(Exp.)	38.21	7.85	0.087	10.464
	(Cal.)	30.36			
ANP		23.42		0.056	6.7356
V		24.00		0.067	8.0587
E$_1$	(Exp.)	12.18	−13.06	0.030	3.6084
	(Cal.)	25.24			
E$_2$	(Exp.)	21.74	−2.48	0.061	7.3370
	(Cal.)	24.22			
SB-2	(Exp.)	28.47	4.76	0.060	7.2167
	(Cal.)	23.71			

Table 2 Excess free energy, excess enthalpy and excess entropy eutectics of 4-chloro-3-nitroaniline (1)–3-hydroxy-4-methoxybenzaldehyde (2) and 4-hydroxy-3-methoxybenzaldehyde (1)–2-amino-4-nitroaniline (2) systems

System	g^E (kJ mol^{-1})	h^E (kJ mol^{-1})	s^E (kJ mol^{-1} K^{-1})
(CNA (1)–HMB (2))			
E$_1$	−0.2078	224.28	0.5953
E$_2$	−0.5315	−22.40	−0.0596
(V (1)–ANP (2))			
E$_1$	0.0146	−5.777	−0.014
E$_2$	0.0948	−16.045	−0.046

between like molecules are stronger than that of unlike molecules. In the case of 4-chloro-3-nitroaniline (1)–3-hydroxy-4-methoxybenzaldehyde (2) system, negative value of excess free energy was observed at each eutectic which indicates that stronger association between unlike molecules. The excess thermodynamic functions of eutectics are reported in Table 2. The roughness parameters were also calculated using earlier reported equations.[50] The values of roughness parameters was found to be $\alpha > 2$ (ref. 42 and 55) in all the cases which indicate that the interface is quite smooth and the crystal developed with a faceted morphology those values are presented in Table 1. Thermal stability of SB-1 and SB-2 are also studied by TGA method. TGA plots of SB-1 and SB-2 are shown in Fig. 3a and b, respectively. The TGA plot of SB-1 showed that it is thermally stable up to 500 K and shows stability after its melting. Fig. 3a indicates that SB-1 is more stable than that of 3-hydroxy-4-methoxybenzaldehyde (HMB) and 4-chloro-3-nitroaniline (CNA). It is clear from Fig. 3b, SB-2 is stable up to 505 K and thermally more stable than that of starting compound 4-hydroxy-3-methoxybenzaldehyde and 2-amino-4-nitrophenol.

3.3. Spectral analyses

3.3.1. ^{1}H and ^{13}C analysis. ^{1}H NMR spectrum of 4-chloro-3-nitroaniline (1)–3-hydroxy-4-methoxybenzaldehyde (2) system, a signal appears at 9.87 ppm (1H, s) which is attributed to the presence of carbonyl ($\rangle$C=O) proton of –CHO group. The 4-chloro-3-nitroaniline shows the signal at 3.99 ppm (2H, s) for –NH$_2$ protons while in SB-1, ^{1}H NMR spectrum, a new signal at 8.33 ppm (1H, s) confirmed that the presence of imine (–CH=N–) proton. In ^{13}C NMR spectrum of 4-chloro-3-nitroaniline, a NMR signal at 132 ppm which is attributed to carbon attached to –NH$_2$ group and 3-hydroxy-4-methoxybenzaldehyde shows a NMR signal at 190 ppm which is due to carbonyl (–CHO) carbon. These both signals disappeared in ^{13}C NMR spectra of synthesized Schiff's bases and a new NMR signal appeared at 162 ppm due to presence of imine (–CH=N–) carbon. This finding indicates that the –NH$_2$ group of 4-chloro-3-nitroaniline reacts with the carbonyl (–CHO) group of 3-hydroxy-4-methoxybenzaldehydeand forms new moiety (–CH=N–) by chemical association. ^{1}H and ^{13}C NMR spectra of SB-1 are shown in Fig. S1a and b.†
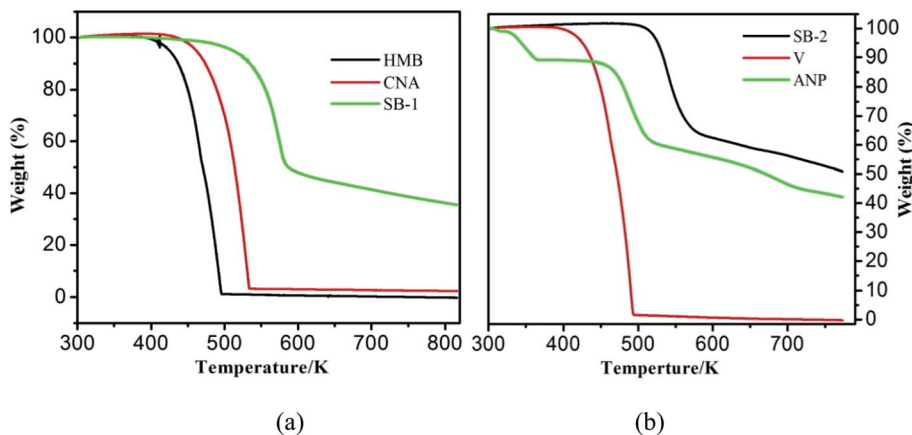
Fig. 3 TGA curves of (a) **SB-1**, HMB and CNA (b) **SB-2**, ANP and vanillin (V).

Table 3 Chemical structure, IUPAC name, molecular formula, m.p., IR and NMR data of **SB-1** and **SB-2**

S. no.	IUPAC name	Chemical structure	Molecular formula, mp and IR and NMR data
1	4-((4-Chloro-3-nitrophenylimino)-methyl)-2-methoxyphenol (**SB-1**)		$C_{14}H_{11}ClN_2O_4$ (mol. wt 306.70), mp – 439 K, IR (KBr) – 1623 cm^{-1}, ^{1}H NMR (300 MHz, CDCl$_3$), δ (ppm); 8.33 (1H, s)
2	2-(4-Hydroxy-3-methoxybenzy-lideneamino)-4-nitrophenol (**SB-2**)		$C_{14}H_{12}N_2O_5$ (mol. wt 288), mp – 474 K, IR (KBr) – 1629 cm^{-1}, ^{1}H NMR (300 MHz, CDCl$_3$), δ (ppm); 8.61 (1H, s)

In case of 4-hydroxy-3-methoxybenzaldehyde (1)–2-amino-4-nitrophenol (2) system, ^{1}H and ^{13}C NMR spectra of **SB-2** have been shown in Fig. S1c and d,† ^{1}H NMR spectrum of 4-hydroxy-3-methoxybenzaldehydeshows NMR signal for –CHO proton at 9.82 ppm (1H, s) and ^{1}H NMR spectrum of 2-amino-4-nitrophenol shows a NMR signal at 5.20 ppm (2H, s) for –NH$_2$ protons. ^{1}H NMR spectrum of **SB-2** furnished a signal at 8.61 ppm (1H, s) for imine (–CH=N–) proton. Presence of new ^{1}H NMR signal at 8.61 ppm (1H, s) in **SB-2** and absence of NMR signals for –CHO and –NH$_2$ protons conformed that the formation of **SB-2**. In ^{13}C NMR spectrum of 4-hydroxy-3-methoxybenzaldehyde, signal at 190 ppm appeared for –CHO carbon and in 2-amino-4-nitrophenol spectrum signal at 137 ppm appeared for carbon attached to the –NH$_2$ group. The ^{13}C NMR spectrum of **SB-2** showed a signal at 162 ppm which is attributed to due to imine (–CH=N–) carbon (Fig. S1d†). These results confirm that the formation of Schiff bases (**SB-1** and **SB-2**). Chemical structure, IUPAC name, molecular formula, m.p. and NMR data of the synthesized **SB-1** and **SB-2** are reported in Table 3.

3.3.2. FT-IR analysis. In FT-IR spectrum, the 4-chloro-3-nitroaniline (1)–3-hydroxy-4-methoxybenzaldehyde (2) system, 4-chloro-3-nitroaniline show two bands at 3225 and 3407 cm^{-1} which is attributed to the symmetric and asymmetric stretching

of –NH$_2$. The 3-hydroxy-4-methoxybenzaldehyde shows band at 1672 cm^{-1} which is due to $\rangle$C=O of –CHO. Spectrum of **SB-1**, shows a band at 1623 cm^{-1} due to the imine (–CH=N–). In 4-hydroxy-3-methoxybenzaldehyde (1)–2-amino-4-nitrophenol (2) system, the spectrum of 2-amino-4-nitrophenol show two bands at 3291 and 3352 cm^{-1} which is attributed to the symmetric and asymmetric stretching of –NH$_2$ group. The spectrum of 4-hydroxy-3-methoxybenzaldehyde shows a band at 1666 cm^{-1} due to carbonyl of –CHO group. In the spectrum of **SB-2** these bands are disappeared and one new band appears at 1629 cm^{-1} due to imine (–CH=N–). The IR analysis confirmed that the formation of both SBs.

3.3.3. Single crystal X-ray diffraction (SCXRD). In case of 4-chloro-3-nitroaniline (1)–3-hydroxy-4-methoxybenzaldehyde (2) system, Schiff base formation occurs in 1 : 1 molar ratio of the parent components. Single crystals of the **SB-1** were grown from the mixed (methanol and water) solvent due to moderate solubility of the **SB-1** in this solvent mixture. Saturated solution of **SB-1** was prepared in the mixed solvent and kept solution for the slow evaporation, within a weak small size and hexagonal shape crystals were harvested. The single crystal XRD pattern indicates that **SB-1** crystallizes in monoclinic crystal system with $P2_1/c$ space group and chemical formula is $C_{14}H_{11}ClN_2O_4$. The nature of the bonding has been confirmed by the SCXRD data. The
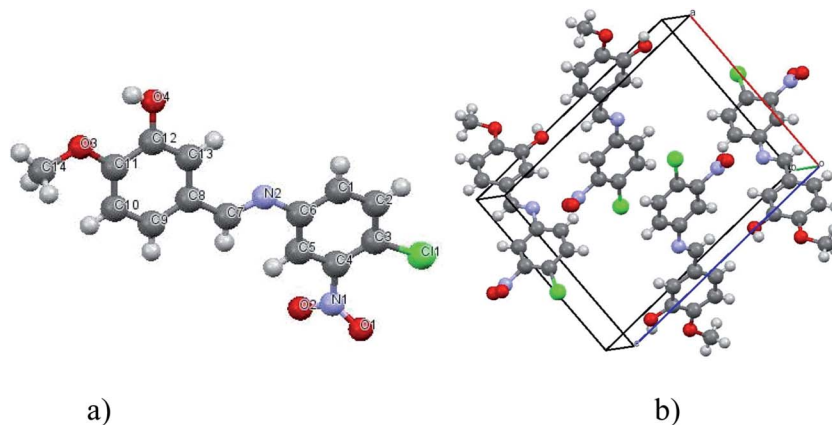
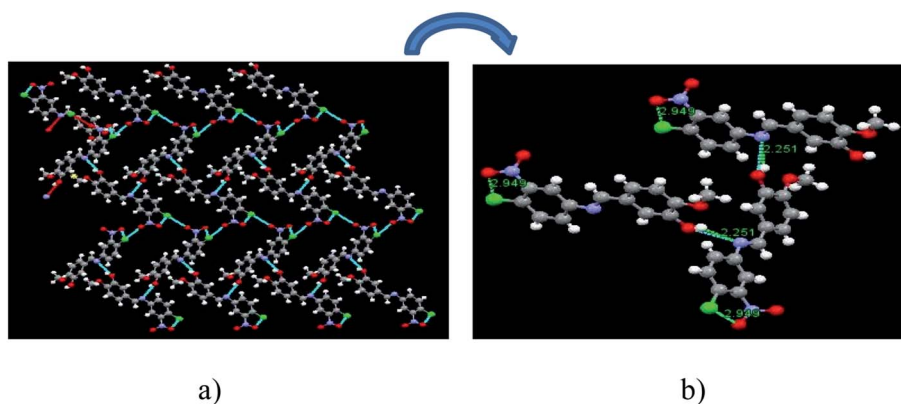**Fig. 4** (a) ORTEP view and numbering scheme and (b) molecular crystal packing in unit cell of **SB-1**.

Fig. 5 (a) Pattern growth of **SB-1** along '*b*' axis and (b) hydrogen bonding interaction between two **SB-1** molecules.

ORTEP and numbering scheme of the **SB-1** is shown in Fig. 4a and unit cell packing shown in Fig. 4b. The hydrogen bonding growth pattern of **SB-1** along '*b*' axis has been shown in Fig. 5a

in which **SB-1** molecules are showing inter molecular hydrogen bonding. The imine (–CH=N–) nitrogen of one **SB-1** molecule shows inter molecular hydrogen bonding with the hydroxyl proton of another **SB-1** molecule which has been shown in Fig. 5b, this provides the extra stability to the **SB-1**. The

Table 4 Crystallographic data and details of refinement of **SB-1**

Formula	$C_{14}H_{11}ClN_2O_4$
F_w	306.70
Crystal system	Monoclinic
Space group	$P2_1/c$
a [Å]	10.5441(2)
b [Å]	9.6460(2)
c [Å]	13.7613(3)
α [1]	90
β [1]	93.6636
γ [1]	90°
V [Å^3]	1396.78(5)
Z	4
D_{calcd} [g cm^{-3}]	1.458 g cm^{-3}
μ (MoK$_\alpha$) [mm^{-1}]	0.291
$F(000)$	632
hkl range	12, 11, 16
T [K]	296
Reflections measured	17 081
Reflections unique	2459
R_{int}	0.09310
GoF (F^2)	1.062

Table 5 Hydrogen bond parameters ([Å] and [α°]) in the crystal of **SB-1**

D–H⋯A	D–H	H⋯A	D⋯A	∠DHA
O_2–H_2⋯O_5	0.820	1.772	2.591	175.98

Table 6 Bond lengths [Å] of the **SB-1** crystal

C1–C2	1.370(4)	C1–C6	1.390(3)
C3–Cl1	1.727(3)	C2–C3	1.380(4)
C4–N1	1.461(3)	C3–C4	1.388(4)
C7–N2	1.272(3)	C4–C5	1.374(4)
C8–C13	1.400(3)	C5–C6	1.389(3)
C11–C12	1.406(3)	C6–N2	1.416(3)
C12–C13	1.363(3)	C7–C8	1.453(3)
C14–O3	1.417(3)	C8–C9	1.387(3)
N1–O1	1.180(4)	C9–C10	1.382(4)
C11–O3	1.365(3)	C10–C11	1.375(3)
C12–O4	1.363(3)	N1–O2	1.202(4)

Table 7 Bond angles [$\alpha°$] of the **SB-1** crystal

C2–C1–C6	121.6(2)	C7–N2–C6	120.8(2)
C2–C3–C4	118.0(2)	C1–C2–C3	120.6(3)
C4–C3–Cl1	122.8(2)	C2–C3–Cl1	119.2(2)
C5–C4–N1	117.0(2)	C5–C4–C3	121.8(2)
C4–C5–C6	120.0(2)	C3–C4–N1	121.2(2)
C1–C6–N2	116.3(2)	C1–C6–C5	118.0(2)
N2–C7–C8	122.9(2)	C5–C6–N2	125.7(2)
C9–C8–C7	119.7(2)	C9–C8–C13	119.0(2)
C10–C9–C8	120.9(2)	C13–C8–C7	121.3(2)
O3–C11–C10	126.5(2)	C11–C10–C9	119.8(2)
C10–C11–C12	119.8(2)	O3–C11–C12	113.6(2)
O4–C12–C11	120.9(2)	O4–C12–C13	119.0(2)
C12–C13–C8	120.3(2)	C13–C12–C11	120.2(2)
O1–N1–C4	119.7(3)	O1–N1–O2	122.6(3)
O2–N1–C4	117.7(3)	C11–O3–C14	118.1(2)

crystallographic data and details of refinement of the crystal are reported in the Table 4. The hydrogen bond parameters are reported in Table 5. The bond lengths and bond angles of the **SB-1** are reported in Tables 6 and 7, respectively.

3.3.4. Powder X-ray diffraction (PXRD). The PXRD pattern of 4-chloro-3-nitroaniline (1)–3-hydroxy-4-methoxybenzaldehyde (2) system is shown in Fig. 6a. The Bragg's peaks of the 3-hydroxy-4-methoxybenzaldehyde, 4-chloro-3-nitroaniline (parent components) and **SB-1** are assigned by using the symbols ($), (@) and (#), respectively. New Bragg's diffraction peaks at 19.00, 19.74, 21.69, 23.37, 28.16 appeared in the PXRD pattern of **SB-1** apart from these the variation in the intensity of the parents and few diffraction peaks of parent components completely disappear. This indicates that the compound is entirely different from its constituents. In the PXRD pattern of E_1, peaks of 3-hydroxy-4-methoxybenzaldehyde and few peaks of compound **SB-1** has appeared while in case of E_2, peaks of 4-chloro-3-nitroaniline as well as **SB-1** are observed this indicates that molecular complex is different compound and behaves as one of the parent component for eutectics.

The PXRD pattern of the systems vanillin (1)–2-amino-4-nitrophenol (2), is shown in Fig. 6b. The Braggs' peaks of vanillin, 2-amino-4-nitrophenol and **SB-2** assigned by symbol (@, $ and *), respectively. Results show that the pattern of **SB-2** is

different from their parent components, new peaks 15.55, 18.40, 23.70, 25.90, 27.98 appear at 2θ value as well as several peaks of parent components disappear. This indicates that **SB-2** is new entity and behaves as one of the parent component for both eutectics E_1 and E_2.

3.3.5. UV-vis absorption. UV-vis spectra of 4-chloro-3-nitroaniline, 3-hydroxy-4-methoxybenzaldehyde and **SB-1** were recorded in the range of 190–900 nm in methanol at the 1×10^{-5} M concentration at room temperature and shown in Fig. 7a. The spectrum of CNA show two bands at 242 and 377 nm due to the $\pi \rightarrow \pi^*$ and $n \rightarrow \pi^*$ transitions, respectively. In the spectrum of HMB two bands appear at 274 and 311 nm due to $\pi \rightarrow \pi^*$ and $n \rightarrow \pi^*$ transitions, respectively. The band at 311 nm because of lone pair electrons of $\rangle C=O$ group. In the spectrum of **SB-1**, two bands appear at 286 and 332 nm, the band at 286 nm is attributed to the $\pi \rightarrow \pi^*$ transition of aromatic electrons and at 332 nm is ascribed to the $\pi \rightarrow \pi^*$ transition due to formation of imine. The peaks of **SB-1** spectrum shows bathochromic as well as hyperchromic shift as compared to HMB parent due to extended conjugation.[56]

In 4-hydroxy-3-methoxybenzaldehyde (1)–2-amino-4-nitrophenol (2) system, absorption spectra are shown in Fig. 7b. The compound ANP shows band at 376 nm due to $n–\pi^*$ transition because of presence of –NH$_2$ group which disappeared in the **SB-2** spectrum. The compound vanillin show two bands one at 276 nm due to $\pi–\pi^*$ transition because of hydroxyl (–OH) group and second at 308 nm due to ($\rangle C=O$) $n–\pi^*$ transition. The 308 nm band appeared due to presence of non-bonded electrons of –CHO group. In the spectrum of **SB-2**, band at 311 nm appears due to $n–\pi^*$ transition. The fluorescence properties of both **SB-1** and **SB-2** have been studied and shown in Fig. 8a and b. **SB-1** shows a weak emission band while **SB-2** shows a band at 313 nm.

3.4. Corrosion inhibition study

3.4.1. Electrochemical studies

3.4.1.1. Open circuit potential. Potential developed over the surface of working electrode (mild steel) with respect to the potential of saturated calomel (reference electrode) without
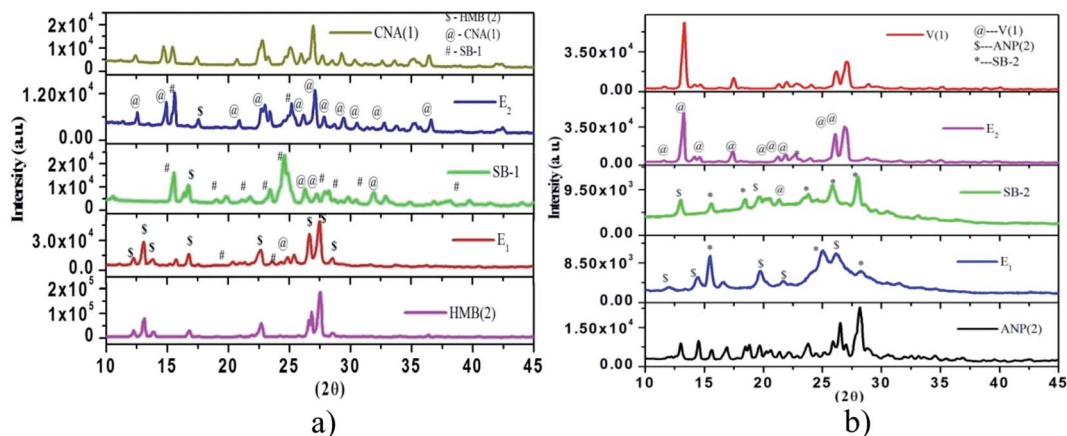

Fig. 6 Powder XRD plots of (a) 4-chloro-3-nitroaniline (1)–3-hydroxy-4-methoxybenzaldehyde (2) and (b) 4-hydroxy-3-methoxybenzaldehyde (1)–2-amino-4-nitrophenol (2) systems.
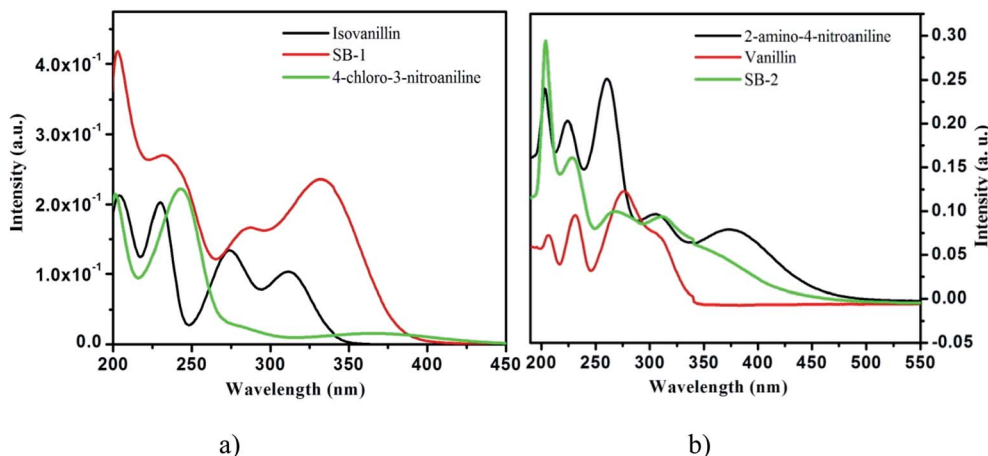
Fig. 7 UV-vis absorption spectra of (a) 4-chloro-3-nitroaniline (1)−3-hydroxy-4-methoxybenzaldehyde (2) and (b) 4-hydroxy-3-methoxybenzaldehyde (1)−2-amino-4-nitrophenol (2) systems.
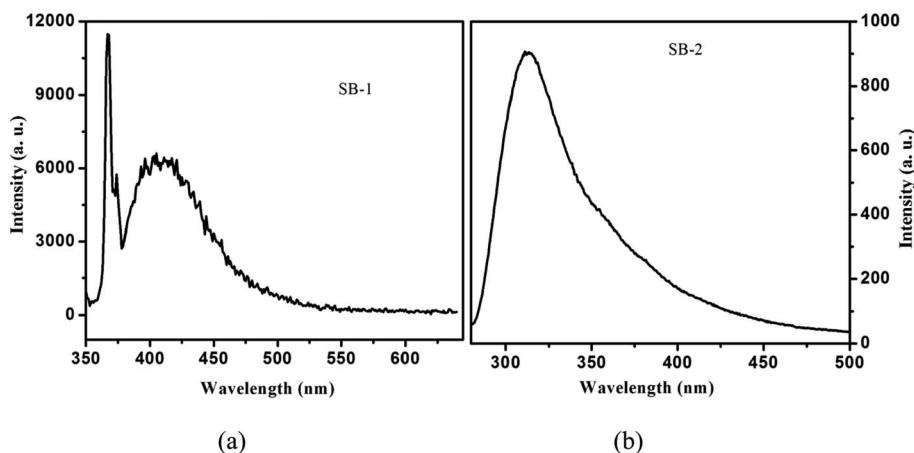

Fig. 8 Fluorescence spectrum of (a) **SB-1** and (b) **SB-2**.

applying any external current is known as open circuit potential (OCP). Fig. 9 depicts the change in the open circuit potential (OCP) of the working electrode in the acidic solution of in 1 M
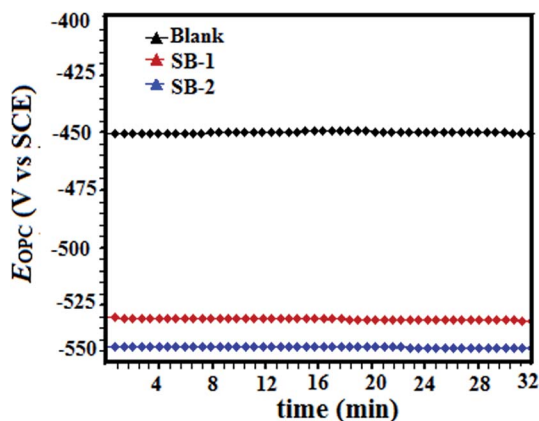

Fig. 9 Variation of open circuit potential for mild steel dissolution in the absence and presence of tested inhibitors with time (minutes).

HCl with and without tested SB molecules at their optimum concentration of 0.327 mM. It can be seen from the figure that after 30 minutes immersion time the OCP *vs.* time plots, in the presence of tested Schiff's bases shifted towards more negative direction without changing common features of the OCP *vs.* time plots. This finding reveals that the surface layer of oxides (Fe_2O_3, Fe_3O_4) has been completely removed and inhibitive layer of inhibitors have been formed.[57,58]

3.4.1.2. Potentiodynamic polarization. Effect of SBs concentration on the electrochemical behaviour of mild steel in 1 M hydrochloric acid has also been studied using electrochemical techniques. Electrochemical polarization curves for mild steel corrosion in the absence and presence of different concentrations of newly synthesized SBs are presented in Fig. 10a and b and various polarization parameters such as corrosion potential (E_{corr}), corrosion current density (i_{corr}), anodic and cathodic Tafel slopes (β_a, β_c) derived from extrapolating the linear segments of anodic and cathodic Tafel slopes are given in Table 8. Inspection of results displayed that the values of corrosion current density (i_{corr}) decreased significantly in the
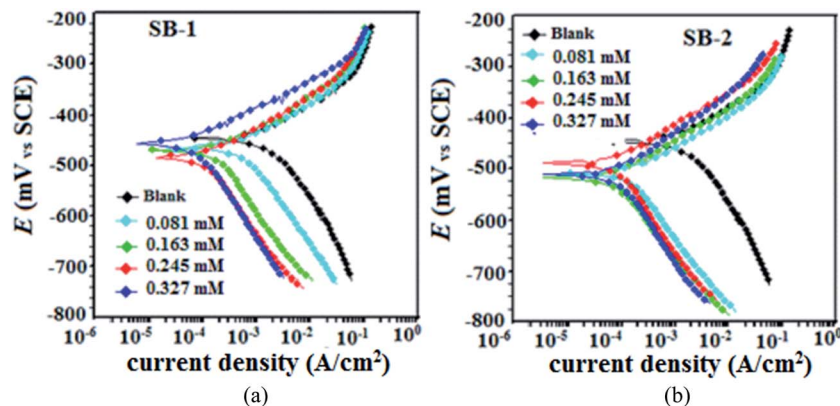
Fig. 10 Potentiodynamic polarization curves for mild in the absence and presence of different concentrations of the studied inhibitors (a) **SB-1** and (b) **SB-2**.

Table 8 Tafel polarization parameters for mild steel in 1 M HCl in the absence and presence of different concentrations of **SB-1** and **SB-2**

Inhibitor	Conc. (mM)	E_{corr} (mV per SCE)	β_a (mV dec^{-1})	$-\beta_c$ (mV dec^{-1})	i_{corr} (μA cm^{-2})	$\eta\%$
Blank	—	−445	70.5	114.6	1150	—
SB-1	0.081	−469	62.4	195.2	432	62.43
	0.163	−483	66.4	219.3	146	87.30
	0.245	−482	58.9	141.9	82.3	92.84
	0.327	−455	55.1	105.8	50.8	95.58
SB-2	0.081	−489	80.6	109.1	286	75.13
	0.163	−511	85.8	189.9	110	90.43
	0.245	−489	75.6	178.8	73.4	93.61
	0.327	−518	69.8	150.7	36.8	96.80

presence of the SBs indicating that they act as good corrosion inhibitors for mild steel in 1 M hydrochloric acid solution. From the results depicted in the Table 8 it can be seen that values of corrosion current densities decrease on increasing the concentration of the both tested SBs and maximum decrease was observed at 0.327 mM concentration. Further increase in the inhibitors concentrations did not changed their inhibition performance which reveals that 0.327 mM is optimum concentration in the for both the studied Schiff's bases molecules. Results further showed that as compared to uninhibited specimen, the inhibited specimens did not showed any significant change in values of E_{corr} as maximum change in E_{corr} values were 38 and 73 mV for **SB-1** and **SB-2**, respectively, indicating that both SBs act as mixed type corrosion inhibitors with predominantly cathodic type in behaviour.[46–48] Careful examination of results (Table 8) reveal that the values of β_c for inhibited test specimens showed more prominent change as compared to value of β_a, with respect to value of Tafel slopes (β_a, β_c) of uninhibited solution. This finding suggests that the studied SBs predominantly affect the mechanism of cathodic hydrogen evolution.[12,46,47] The maximum decrease in i_{corr} values of 50.8 and 36.8 mA cm^{-2} were obtained for **SB-1** and **SB-2**, respectively at as low as 0.327 mM concentration.

3.4.1.3. EIS study. The Nyquist and Bode plots for the mild steel corrosion in the absence and presence of studied concentrations of **SB-1** and **SB-2** are shown in Fig. 11(a and b)

and 12(a and b), respectively. The inhibited and uninhibited Nyquist plots depict a single semicircle loop suggesting that corrosion of mild steel in acid solution is a charge transfer phenomenon which is further supported by single maxima in the Bode plots. Furthermore, Nyquist plots show some inductive loop in the low frequency regions which is attributed to the relaxation adsorbed inhibitor molecules on the metallic surface.[59,60] In present investigation all the EIS data were analyzed using an equivalent circuit shown in Fig. 11c. This circuit contains polarization resistance (R_p), solution resistance (R_s) and a constant phase element (CPE). In present analysis difference in the real impedance at lower and higher frequencies depicted as polarization resistance (R_p) rather than more commonly used charge transfer resistance (R_{ct}). The criterion behind using R_p is based on the fact that the metal corroding in aqueous solution is generally associated with other types of resistances such as diffusion resistance (R_d), accumulation resistance (R_a) and film resistance (R_f) along with charge transfer resistance (R_{ct}) *i.e.* $R_p = R_d + R_a + R_f + R_{ct}$.[61–63] From Fig. 11(a and b) it is apparent that diameter of the Nyquist plots in presence of studied SBs are higher than in their absence indicating that inhibition of metallic corrosion occurs *via* formation of protective film at metal/electrolyte interfaces.[46–63] Several electrochemical impedance parameters such as R_s (solution resistance), polarization resistance (R_p), and phase shift (n) double layer capacitance (C_{dl}) were derived using
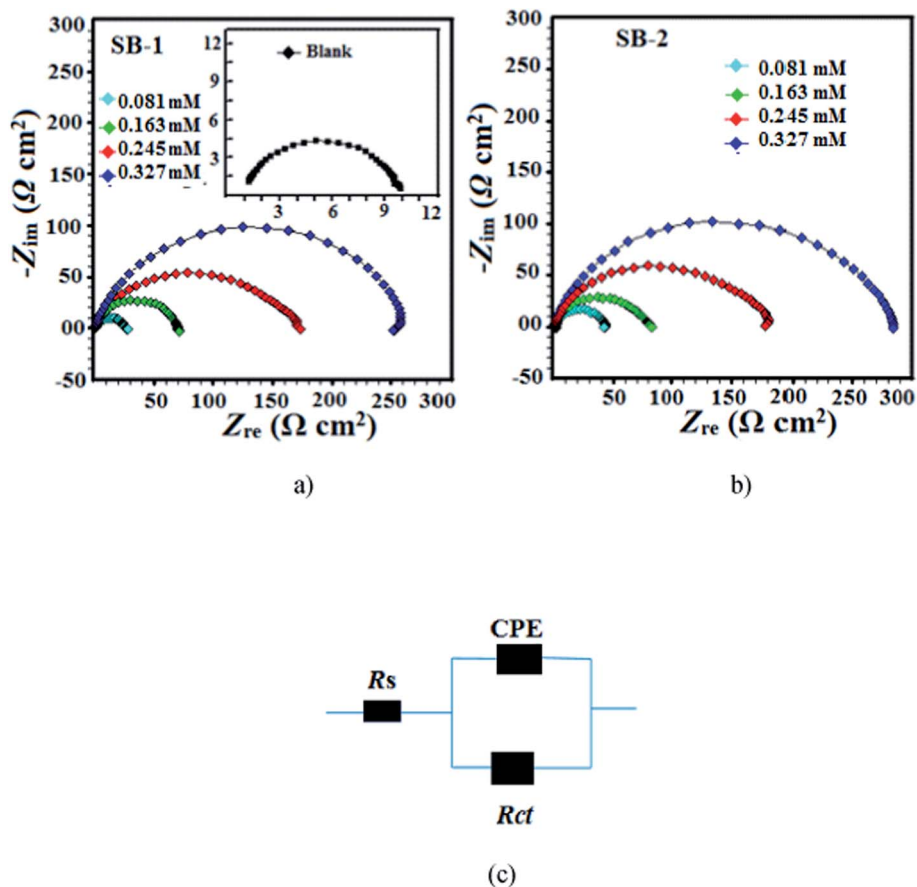
Fig. 11 Nyquist plot for mild steel in 1 M HCl in the absence and presence of different concentrations of (a) **SB-1** and (b) **SB-2**. (c) Equivalent circuit used for the analysis of the EIS data.
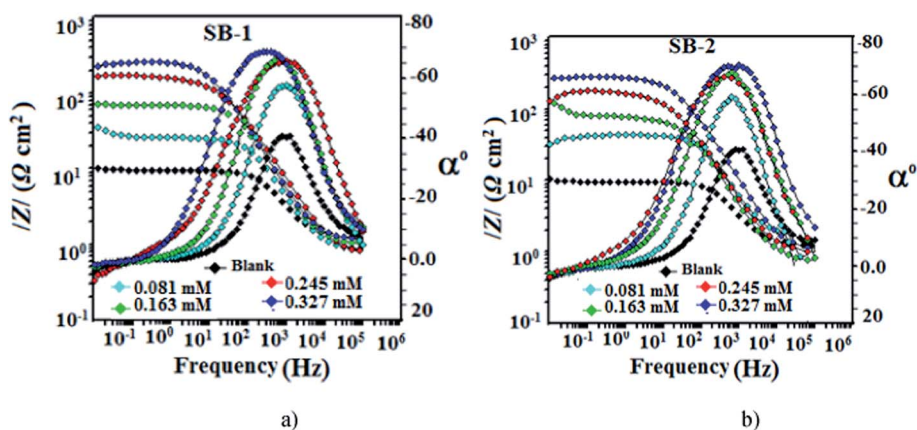

Fig. 12 Bode plots for mild steel in 1 M HCl in the absence and presence of different concentrations of (a) **SB-1** and (b) **SB-2**.

equivalent circuit and presented in Table 9. The inhibition efficiencies at different studied concentration have been evaluated using eqn (2) and are also summarized in the same table. In general, for a metal corroding system, CPE is being utilized rather than pure capacitor due to the presence of surface in homogeneity. Impedance of the CPE (Z_{CPE}) can be represented by following equation:[46,47]

$$Z_{CPE} = \left(\frac{1}{Y_0}\right)\left[(j\omega)_n\right]^{-1} \tag{12}$$

where, Y_0, n, ω and j represent CPE constant, phase shift, angular frequency and imaginary number, respectively. Higher value of phase shift is associated with high surface smoothness and *vice versa*. In addition, to the surface in homogeneity value of n can also be employed for studied the nature of impedance

Table 9 EIS parameters for mild steel in 1 M HCl in the absence and presence of different concentrations of SBs

Inhibitor	Conc.	R_s (Ω cm^2)	R_p (Ω cm^2)	Y_0	n	C_{dl} (μF cm^{-2})	$\eta\%$
Blank	—	1.12	9.58		0.827	106.21	—
SB-1	0.081	0.844	26.08	156.0	0.837	56.43	63.30
	0.163	1.000	68.95	96.7	0.868	41.94	86.10
	0.245	0.716	164.3	136.2	0.844	38.05	91.93
	0.327	1.121	250.9	102.3	0.832	35.90	96.18
SB-2	0.081	1.133	40.23	87.6	0.871	38.95	76.18
	0.163	0.838	81.80	96.3	0.837	34.83	88.28
	0.245	0.957	166.3	89.6	0.838	32.60	94.23
	0.327	1.034	276.3	61.2	0.847	23.50	96.53

spectra as value of $n = 0$, 1, -1, and 0.5 represent resistance, capacitance, inductance and Warburg impedance, respectively.[12,46–48] In present study, values of n in the presence and absence of studied SBs varies from 0.827 to 0.871 and are slightly deviated from unity (ideal capacitor). This type of deviation from ideal capacitive behaviour is attributed to the surface in homogeneity caused from structural and interfacial origin.[12,43–45] In the present study, values of double layer capacitance (C_{dl}) are derived using following relationship:[46–48]

$$C_{dl} = Y_0[(\omega)_{max}]^{n-1} \quad (13)$$

where, ω_{max} denotes frequency at which imaginary part of impedance is maximum (rad s^{-1}). The careful examination of results depicted in Table 9 it shows that values of R_p increased and values of C_{dl} decreased in the presence of SBs particularly at higher SBs concentrations. The increase in values of R_p and decrease in value of C_{dl} indicate that both SBs adsorbed at the metal/electrolyte interfaces and thereby increased thickness of electric double layer and inhibit acidic mild steel corrosion.[12,46–63]

The adsorption of the SBs on the metal/electrolyte interfaces and non-ideal capacitive behaviour of impedance spectra have also been supported by Bode plots (Fig. 12a and b). An ideal capacitor is characterized by a constant slope value of -1 and phase angle of 90°.[12,46–48] However, in present investigation, slight deviation is observed from the ideal capacitive behaviour as values of slopes and phase angles are not equal to their corresponding ideal values. Deviation from the ideal capacitor is again attributed to surface roughness. However, it can be seen that values of phase angles increased significantly in the presence of SBs suggesting that surface morphology of inhibited specimens have been smoothened remarkably due to adsorption of SBs on metallic surface.[12,14,46–48]

3.4.2. Adsorption isotherm. Generally, organic inhibitors act by adsorbing on the interfaces of metal and electrolyte that result into formation of protective barrier for corrosion process. Behaviour and mode of adsorption can be determined through several commonly used isotherms such as Temkin, Frumkin, Freundlich and Langmuir adsorption isotherms. In present study, out of several tested isotherms, Langmuir adsorption isotherm represents the best fit with value of regression coefficient (R^2) close to one (Fig. 13). The Langmuir adsorption isotherm can be presented as:[12]

$$K_{ads}C = \frac{\theta}{1-\theta} \quad (14)$$

where, θ is the surface coverage, K_{ads} is the equilibrium constant of adsorption–desorption processes taking place over metallic surface and C is the equilibrium inhibitor concentration. Values of the K_{ads} were in the order of 10^4 suggesting that these inhibitor molecules have strong interaction with the metal in acid solution. Free energy of adsorption (ΔG_{ads}) for mild steel corrosion was calculated using the following expression:[12]

$$\Delta G_{ads} = -RT \ln(55.5K_{ads}) \quad (15)$$

where, K_{ads} is the equilibrium binding constant, T is temperature and R is gas constant. Generally a higher value of K_{ads} results into the stronger adsorption. The negative value of Gibb's free energy of adsorption in the present case indicates that adsorption of studied SBs on mild steel is a spontaneous process. In general, values of $\Delta G_{ads} \leq 20$ kJ mol^{-1} is resulted in to the electrostatic interaction (physical adsorption) between charged inhibitor molecules and metal whereas values of $\Delta G_{ads} \leq 40$ kJ mol^{-1} involve transfer charges from the inhibitor molecules to mild steel surface in order to form covalent bond (chemisorption). In present study, the ΔG_{ads}
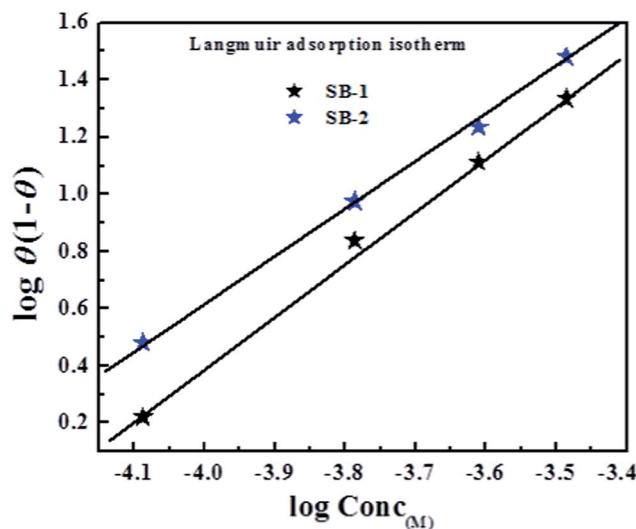

Fig. 13 Langmuir adsorption isotherm plots for adsorption of investigated Schiff's bases (SBs) on mild steel surface in 1 M HCl solution.
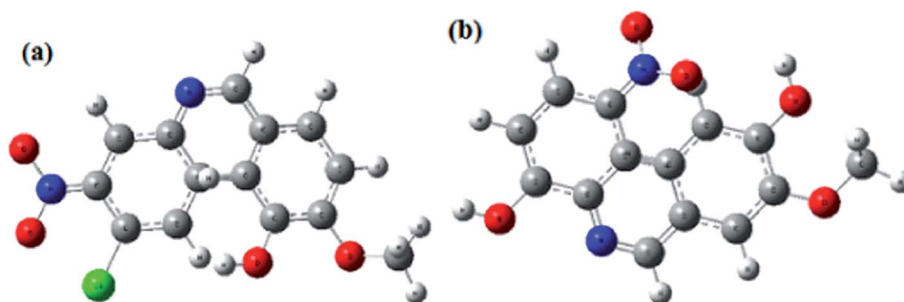
Fig. 14 Optimized molecular structures of (a) **SB-1** and (b) **SB-2** at B3LYP/6-31+(d,p) level of theory.
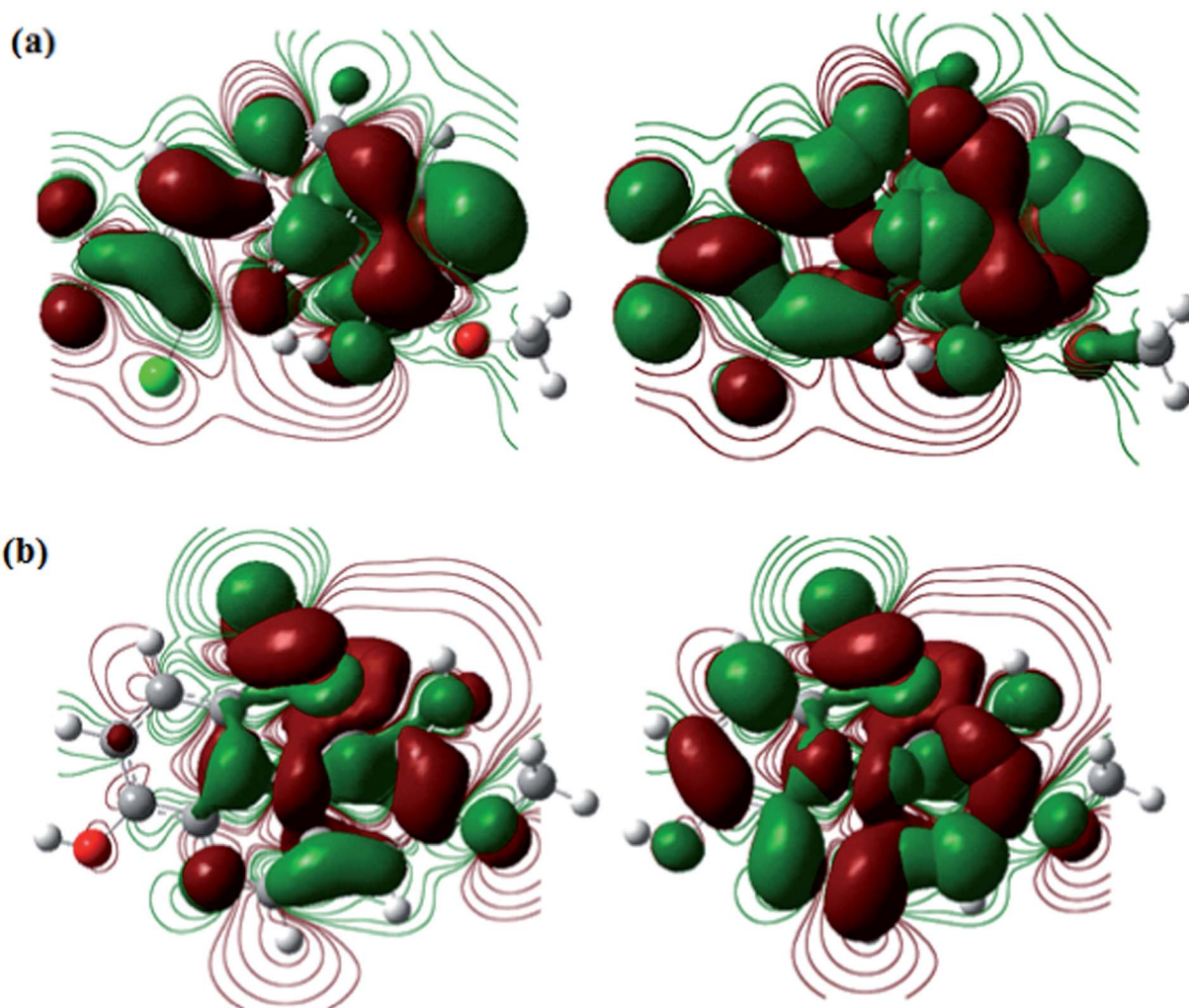

Fig. 15 The frontier molecular orbital (left-hand side: HOMO; and right-hand side: LUMO) of the studied SBs (a) **SB-1** and (b) **SB-2**.

values ranged from −34 kJ mol⁻¹ to −38 kJ mol⁻¹. Since, the values of ΔG_{ads} are more close to −40 kJ mol⁻¹ (chemisorption) as compared to the −20 kJ mol⁻¹ (physisorption) and therefore it is concluded that adsorption of the tested compounds on the mild steel surface in 1 M HCl follows predominantly chemisorption mechanism.[64,65]

3.4.3. DFT analysis. DFT based quantum chemical calculations were also performed on the studied SBs in order to derive some more insight in to their inhibition and adsorption behaviour. The optimized structures of both SBs and their frontier molecular electron (HOMO and LUMO) distribution are shown in Fig. 14(a and b) and 15(a and b), respectively. From Fig. 14, it is observed that frontier electron distributions of

Table 10 DFT based quantum chemical calculations parameters derived for neutral form of the inhibitors

Inhibitors	Parameters						
	E_{HOMO} (hartree)	E_{LUMO} (hartree)	ΔE (hartree)	χ	η	σ	ΔN
SB-1	−0.25586	−0.23111	0.02475	0.243485	0.012375	80.80808	2.6951
SB-2	−0.24444	−0.23063	0.01381	0.237535	0.006905	144.8226	4.3768

HOMO and LUMO are localized almost on entire part of the molecules indicating that entire part of molecules is involved in electron transfer (HOMO) and acceptance (LUMO).[66–68] Several theoretical parameters have also been derived and listed in Table 10. In general, value of E_{HOMO} and E_{LUMO} related with electron donating and accepting tendency of the molecule, respectively. A higher value of E_{HOMO} and lower value of E_{LUMO} is consistent with high inhibition efficiency. In our present study, both the studied inhibitors obeyed the order of E_{HOMO} and E_{LUMO}. It is reported that an organic species with high chemical reactivity *i.e.* lower energy band gap (ΔE; $E_{LUMO} - E_{HOMO}$) is associated with high inhibition efficiency. In present study, values of ΔE followed the order: SB-2 > SB-1, which is consistent with order of inhibition efficiency obtained by electrochemical measurements.[12,46–48] The electronegativity (χ) is another important parameter which can be directly correlated with the inhibition efficiency of inhibitors. High value of χ indicates lower electron donating ability and ultimately lower inhibition efficiency and *vice versa*. SB-2 has lower value of χ (0.237535) as compared to SB-1 (0.243485) suggesting that SB-2 more readily transfers its electrons to d-orbital of the surface Fe atoms as compared to SB-1 resulting in high inhibition efficiency of SB-2.[12,46–48,66–68] The electron transfer ability of the organic compounds also depends upon the values of global hardness (η) and softness (σ). A chemical species with lower value of η or higher value of σ is related with high chemical reactivity and thereby high inhibition efficiency.[12,46–48,66–68] Values of η and σ, in present study obey the experimental order of inhibition efficiency. Lastly, values of fraction of electron transfer (ΔN) for both inhibitor molecules have been derived in order to corroborate the experimental results. It is important to mention that adsorption of organic inhibitors on metallic surface involves electron transfer and therefore, higher value of ΔN suggest high electron transfer and thereby high adsorption tendency. Values of ΔN follow the order: SB-2 (1.427238) > SB-1 (0.555966), which supports the order of experimental inhibition efficiency.[12,46–48,66–68]

4. Conclusions

Two novel Schiff bases (SBs) namely; 5-((4-chloro-3-nitrophenylimino)methyl)-2-methoxyphenol (SB-1) and 2-(4-hydroxy-3-methoxybenzylidineamino)-4-nitrophenol (SB-2). Solid–liquid phase have been synthesized and investigated as effective corrosion inhibitors for mild steel in 1 M HCl. Investigated SBs were characterized by their spectral analyses (^{1}H and ^{13}C NMR and FT-IR). Single crystal XRD study of SB-1 reveals

that it crystallizes in monoclinic unit cell with $P2_1/c$ space group. The DSC and TGA study show SB-1 and SB-2 are highly stable than that of their starting compounds. DSC curves of SB-1, SB-2 show the no other phase transition occurs. TGA curve of SB-1 and SB-2 indicates that both are stable after their melting temperature and information about the decomposition behavior. Results showed that SB-2 shows better fluorescence property as compared to the SB-1. The EIS and PDP studies suggest that investigated SBs act as efficient inhibitors for mild steel corrosion in 1 M HCl and showed maximum efficiencies of 95.58% and 96.80% for SB-1 and SB-2, respectively at very low concentration of 0.327 mM. Polarization results showed investigated SBs act as mixed corrosion inhibitors with slight cathodic dominance. Several DFT based quantum chemical parameters supported the order of inhibition efficiency obtained by experimental means. Both experimental and DFT results well complemented each other.

Conflicts of interest

The authors declare no conflict of interest of any form.

Acknowledgements

References

1 S. M. A. Hosseini, M. Salari, E. Jamalizadeh, S. Khezripoor and M. Seif, *Mater. Chem. Phys.*, 2010, **119**, 100–105.

2 M. A. Quraishi, A. Singh, V. K. Singh, D. K. Yadav and A. K. Singh, *Mater. Chem. Phys.*, 2010, **122**, 114–122.

3 I. B. Obot and N. O. Obi-Egbedi, *Corros. Sci.*, 2010, **52**, 282–285.

4 Special Issue, NACE, *Materials Performance*, Houston, Texas, USA, July 2002.

5 Confederation of Indian Industry, *1st Global Corrosion Summit*, New Delhi, India, 2011.

6 R. K. Gupta, M. Malviya, C. Verma and M. A. Quraishi, *Mater. Chem. Phys.*, 2017, **198**, 360–373.

7 C. Verma, E. E. Ebenso and M. A. Quraishi, *J. Mol. Liq.*, 2017, **233**, 403–414.

8 O. Olivares-Xometl, N. V. Likhanova, M. A. Domínguez-Aguilar, J. M. Hallen and E. Arce, *Appl. Surf. Sci.*, 2006, **252**, 2139–2152.

9 C. Verma, L. O. Olasunkanmi, E. E. Ebenso, M. A. Quraishi and I. B. Obot, *J. Phys. Chem. C*, 2016, **120**, 11598–11611.

10 O. Olivares-Xomet, N. V. Likhanova, M. A. Domınguez-Aguilar, E. Arcec, H. Dorantes and P. Arellanes-Lozada, *Mater. Chem. Phys.*, 2008, **110**, 344–351.

11 O. Olivares, N. V. Likhanova, B. Gomez, J. Navarrete, M. E. Llanos-Serrano, E. Arce and J. M. Hallen, *Appl. Surf. Sci.*, 2006, **252**, 2894–2909.

12 C. Verma, M. A. Quraishi and A. Singh, *J. Taibah Univ. Sci.*, 2016, **10**, 718–733.

13 M. Rodriguez, G. R. Ortiz, J. L. Maldonado, V. M. H. Ambriz, O. Dominguez, R. Santillan, N. Farfan and K. Nakatani, *Spectrochim. Acta, Part A*, 2011, **79**, 1757–1761.

14 S. Vijayalakshmi and S. Kalyanaraman, *Opt. Mater.*, 2013, **35**, 440–443.

15 D. Sinha, A. K. Tiwari, S. Singh, G. Shukla, P. Mishra, H. Chandra and A. K. Mishra, *Eur. J. Med. Chem.*, 2008, **43**, 160–165.

16 C. M. da Silva, D. L. da Silva, L. V. Modolo, R. B. Alves, M. A. de Resende, C. V. B. Martins and A. de Fatima, *J. Adv. Res.*, 2011, **2**, 1–8.

17 N. S. Gwaram and P. Hassandarvish, *J. Appl. Pharm. Sci.*, 2014, **10**, 75–80.

18 S. Chatterjee and S. Bhattacharyya, *Asian J. Biochem. Pharm. Res.*, 2015, **4**, 2231–2560.

19 L. Shi, H. M. Ge, S. H. Tan, H. Q. Li, Y. C. Song, H. L. Zhu and R. X. Tan, *Eur. J. Med. Chem.*, 2007, **42**, 558–564.

20 M. M. Abd-Elzaher, A. A. Labib, H. A. Mousa, S. A. Moustafa, M. M. Ali and A. A. El-Rashedy, *J. Basic Appl. Sci.*, 2016, **5**, 85–96.

21 H. Q. Chang, L. Jia, J. Xu, T. F. Zhu, Z. Q. Xu, R. H. Chen, T. L. Ma, Y. Wang and W. N. Wu, *J. Mol. Struct.*, 2016, **1106**, 366–372.

22 Y. Zhou, H. Zhou, T. Ma, J. Zhang and J. Niu, *Spectrochim. Acta, Part A*, 2012, **88**, 56–59.

23 G. Ceyhan, M. Tumer, M. Kose, V. McKee and S. Akar, *J. Lumin.*, 2012, **132**, 2917–2928.

24 Y. Zhou, H. Zhou, T. Ma, J. Zhang and J. Niu, *Spectrochim. Acta, Part A*, 2012, **88**, 56–59.

25 M. Rodrigueza, G. R. Ortiza, J. L. Maldonadoa, V. M. H. Ambriza, O. Dominguezb, R. Santillanb, N. Farfanc and K. Nakatani, *Spectrochim. Acta, Part A*, 2011, **79**, 1757–1761.

26 N. K. Gupta, C. Verma, M. A. Quraishi and A. K. Mukherjee, *J. Mol. Liq.*, 2016, **215**, 47–57.

27 K. C. Emregül and O. Atakol, *Mater. Chem. Phys.*, 2003, **82**, 188–193.

28 T. Sethi, A. Chaturvedi, R. K. Upadhyay and S. P. Mathur, *J. Chil. Chem. Soc.*, 2007, **52**, 1206–1213.

29 N. Soltani, M. Behpour, S. M. Ghoreishi and H. Naeimi, *Corros. Sci.*, 2010, **52**, 1351–1361.

30 D. Zheng, C. Hu, T. Gan, X. Dang and S. Hu, *Sens. Actuators, B*, 2010, **148**, 247–252.

31 M. W. Sabaa, R. R. Mohamed and E. H. Oraby, *Eur. Polym. J.*, 2009, **45**, 3072–3080.

32 S. Chigurupati, *J. Med. Biol. Eng.*, 2015, **4**(5), 363–366.

33 S. Ghosh and C. M. Reddy, *CrystEngComm*, 2012, **14**, 2444–2453.

34 Y. M. Hijji, B. Barare, A. P. Kennedy and R. Butcher, *Sens. Actuators, B*, 2009, **136**, 297–302.

35 L. Yang, W. Zhu, M. Fang, Q. Zhang and C. Li, *Spectrochim. Acta, Part A*, 2013, **109**, 186–192.

36 A. R. Jimenez, R. L. García, A. C. Lozada, S. Hernandez, T. R. Apan, A. N. Camacho and E. Gomez, *J. Organomet. Chem.*, 2013, **738**, 10–19.

37 R. M. Ahmed, E. I. Yousif and M. J. A. Jeboori, *Sci. World J.*, 2013, **2013**, 754868.

38 S. Issaadi, T. Douadi, A. Zouaoui, S. Chafaa, M. A. Khan and G. Bouet, *Corros. Sci.*, 2011, **53**, 1484–1488.

39 K. C. Emregul and O. Atakol, *Mater. Chem. Phys.*, 2003, **82**, 188–193.

40 M. A. Hegazy, *Corros. Sci.*, 2009, **51**, 2610–2618.

41 N. B. Singh, S. S. Das, P. Gupta and M. K. Dwivedi, *J. Cryst. Growth*, 2008, **311**, 118–122.

42 R. K. Gupta and R. A. Singh, *J. Cryst. Growth*, 2004, **267**, 340–347.

43 T. Agrawal, P. Gupta, S. S. Das, A. Gupta and N. B. Singh, *J. Chem. Eng. Data*, 2010, **55**, 4206–4210.

44 G. M. Sheldirck, *Shelex-97, Program for Crystal Structure Refinement from Diffraction Data*, University of Gottingen, Gottingen, 1997.

45 J. Haque, V. Srivastava, C. Verma and M. A. Quraishi, *J. Mol. Liq.*, 2017, **225**, 848–855.

46 C. Verma, L. O. Olasunkanmi, I. B. Obot, E. E. Ebenso and M. A. Quraishi, *RSC Adv.*, 2016, **6**, 53933–53948.

47 N. K. Gupta, C. Verma, M. A. Quraishi and A. K. Mukherjee, *J. Mol. Liq.*, 2016, **215**, 47–57.

48 H. Keles, D. M. Emir and M. Keles, *Corros. Sci.*, 2015, **101**, 19–31.

49 Z. Cao, Y. Tang, H. Cang, J. Xu, G. Lu and W. Jing, *Corros. Sci.*, 2014, **83**, 292–298.

50 S. K. Saha, A. Dutta, P. Ghosh, D. Sukul and P. Banerjee, *Phys. Chem. Chem. Phys.*, 2016, **18**, 17898–17911.

51 A. Kokalj, *Chem. Phys.*, 2012, **393**, 1–12.

52 S. K. Saha, M. Murmu, N. C. Murmu and P. Banerjee, *J. Mol. Liq.*, 2016, **224**, 629–638.

53 S. K. Saha and P. Banerjee, *RSC Adv.*, 2015, **5**, 71120–71130.

54 R. S. B. Reddi, V. S. A. K. Satuluri, U. S. Rai and R. N. Rai, *J. Therm. Anal. Calorim.*, 2012, **107**, 377–385.

55 N. B. Singh, S. S. Das, P. Gupta and A. Gupta, *J. Cryst. Growth*, 2008, **311**, 118–122.

56 P. Gupta, T. Agrawal, S. S. Das and N. B. Singh, *J. Chem. Thermodyn.*, 2012, **48**, 291–299.

57 P. S. Kalsi, *Spectroscopy of Organic Compounds*, New Age Publication, India, 6th edn, 2005.

58 X. Li, S. Deng and X. Xie, *Corros. Sci.*, 2014, **81**, 162–175.

59 G. Karthik and M. Sundaravadivelu, *Egypt. J. Pet.*, 2016, **25**, 183–191.

60 F. Bentissa, M. Traisnelb and M. Lagrenee, *Corros. Sci.*, 2000, **42**, 127–146.

61 R. Solmaza, G. Kardas, M. Çulha, B. Yazıcı and M. Erbil, *Electrochim. Acta*, 2008, **53**, 5941–5952.

62 R. Solmaz, *Corros. Sci.*, 2010, **52**, 3321–3330.

63 C. Verma, M. A. Quraishi, E. E. Ebenso, I. B. Obot and A. El Assyry, *J. Mol. Liq.*, 2015, **219**, 647–660.

64 R. Solmaz, *Corros. Sci.*, 2014, **81**, 75–84.

65 R. Solmaz, *Corros. Sci.*, 2014, **79**, 169–176.

66 G. Gece, *Corros. Sci.*, 2008, **50**, 2981–2992.

67 I. B. Obot, S. Kaya, C. Kaya and B. Tuzun, *Phys. E*, 2016, **80**, 82–90.

68 S. Kaya, L. Guo, C. Kaya, B. Tüzüna, I. B. Obot, R. Touir and N. Islam, *J. Taiwan Inst. Chem. Eng.*, 2016, **65**, 522–529.